J Braz. Soc. Mech. Sci. Eng. (2016) 38:2161–2171
DOI 10.1007/s40430-015-0337-1

TECHNICAL PAPER

Nusselt number correlation for synthetic jets

M. V. Lehnen[1] · C. Y. Y. Lee[1] · F. L. D. Alves[1]

Received: 14 November 2014 / Accepted: 10 March 2015 / Published online: 25 March 2015

Abstract Among its many applications, synthetic jets have received much consideration as devices with the ability to enhance or even replace more conventional forced convection cooling techniques. This enhanced cooling is a result of the increase in turbulent mixing brought about by the oscillatory nature of the jet. In this study, the cooling effect of a single synthetic jet impinging directly on a heated surface is examined in a 2-D numerical simulation. Several test cases were examined involving changes in the distance between the heated surface and the jet source, jet Reynolds number, pulsing frequency and Prandtl number. Examination of the timed-averaged velocity field confirms that the synthetic jet forms a circulation cell similar to a steady jet but with more fragmented vorticity. Instantaneous contours of the temperature field also demonstrate the ability of the synthetic jet to redistributed incoming heat through the circulation cell more efficiently than a steady jet. Data from all test cases was reduced through a minimization problem to form a Nusselt number correlation involving the previously mentioned parameters.

Keywords Synthetic jets · Cooling · Computational fluid dynamics

Technical Editor: Francisco Ricardo Cunha.

✉ C. Y. Y. Lee
conrady@unisinos.br

[1] UNISINOS, Av. Unisinos 950, São Leopoldo, RS 93022-000, Brazil

1 Introduction

Synthetic jets are devices formed by a cavity sealed on one side by a plate with a small orifice in one end and a moving membrane in the other [1–4]. The membrane oscillation results in a continuous movement of fluid in and out of the cavity, with the external medium itself providing the necessary source fluid. This characteristic of synthetic jets allows the construction of devices of reduced size and weight and benefit from a low operational cost and flexibility in shape and design [5]. The synthetic jet itself is formed in the blowing phase of the membrane oscillation, as the flow separates on the orifice lips and forms vortical structures. As the membrane reverses oscillation, the ejected vortices have displaced far enough from the orifice to not be drawn back inside the cavity [6, 7]. In this manner, continuous membrane actuation results in a jet with mean momentum away from the orifice and average properties similar to a steady jet.

On the heat transfer side, current electronic cooling techniques are based on forced convection through heat exchangers with air as the working fluid due to its reasonable balance between reliability and cost. However, it has been noted that such conventional methods require fans able to provide a sufficient volumetric airflow rate and pressure difference to circulate air through the network of channels and fins that make up the heat exchanger [8, 9]. This presents a design challenge due to the increasing thermal load generated by ever faster and more densely packed electronic components. Consequently, it is of particular interest to analyze techniques that can improve the heat transfer capabilities of air as a working fluid if this technique is to remain useable in the near future. To this end, synthetic jets are viewed as practical de-vices that can increase convection heat

transfer due to its ability to increase turbulence mixing. Furthermore, the zero-net-mass-flow characteristic of a synthetic jet makes these devices specially suited to integration directly in the electronic component matrix without the need of an external fluid source. Synthetic jet impingement results in a substantial increase in heat transfer and mass flow in a region containing the impact zone [10]. The turbulence enhancing characteristics of vortical structures associated with synthetic jets have been confirmed: when compared to a steady jet, a synthetic jet emitted from the same orifice and with the same jet Reynolds number directed at a surface heated by a constant heat flux resulted in Nusselt numbers up to 3 times larger [11, 12]. The increase in heat transfer is not limited to a jet impinging geometry. Configurations have been tested in which synthetic jets were directed along plates similar to fins in a heat exchanger. When compared to a single fan providing the same average air flow rate, the synthetic jets resulted in a convection coefficient 2.5 times larger and an overall 40 % increase in thermal dissipation in the plates [13–15].

Despite the well documented advantages of synthetic jets, further studies are still required to determine the optimum configuration and operating parameters that will result in the most heat transfer enhancement. In an impingement cooling configuration, the cooling effect was found to be directly dependent on the number of actuators and an optimum spacing distance between them [16]. The synthetic jet performance itself is dependent on the pulsing frequency, which is dependent itself on ressonant frequencies of the device. Two peak jet velocities were found to occur when the device operated at distinct frequencies, corresponding to the membrane natural frequency and the Helmholtz frequency [17]. The effect of some of these parameters were taken in consideration to form a correlation for Nusselt number based on the Reynolds number, Prandtl number, orifice diameter, heated region diameter and distance between the orifice and the heated region [18]. Although acknowledged in [18], the effect of pulsing frequency was not taken in account when determining the Nusselt number correlation.

The work presented here seeks to further expand on the available body of knowledge in the cooling effect of synthetic jets. The main objective of this study was to determine a Nusselt number correlation incorporating geometric parameters such as the distance between the orifice and a heated plate, flow parameters through the Reynolds and Prandtl numbers and operating parameters such as pulsing frequency through the Strouhal number. In order to accomplish this objective, appropriate validation of the numerical approach was carried out at first, followed by extensive test cases in order to collect sufficient data.

2 Governing equations

The governing equations consist of the Reynolds-averaged continuity and Navier–Stokes equations applied to an incompressible fluid with constant thermal properties and no buoyancy. In index notation, theses are shown in Eqs. (1) and (2):

$$\frac{\partial U_i}{\partial x_i} = 0 \tag{1}$$

$$\frac{\partial U_i}{\partial t} + U_j \frac{\partial U_i}{\partial x_j} = -\frac{1}{\rho}\frac{\partial P}{\partial x_i} + (\nu + \nu_T)\frac{\partial^2 U_i}{\partial x_j^2} \tag{2}$$

where U_i is the time averaged velotiy field, x_i is the Cartesian space, ρ is the density, ν is kinematic viscosity of the fluid and ν_T is the turbulent kinematic viscosity.

The energy equation considered is in the form of thermal energy without viscous dissipation or external sources. In a fluid with constant thermal properties this takes the form of (3):

$$\frac{\partial T}{\partial t} + \frac{\partial (U_i T)}{\partial x_j} = \frac{\partial}{\partial x_j}\left[(\alpha + \alpha_T)\frac{\partial T}{\partial x_j}\right] \tag{3}$$

where T is the average temperature fied, α is the thermal diffusivity and α_T is the turbulent thermal diffusivity.

The Shear Stress Turbulence model [19] was selected due to its widely acknowledged ability to resolve inner boundary details (needed for the heat transfer at the wall) and performance in adverse pressure gradients and separated flow (needed to resolve the jet plume). In this model, the turbulent kinematic viscosity is given by (4):

$$\nu_T = \frac{a_1 k_e}{\max(a_1 \omega, SF_2)} \tag{4}$$

where $a_1 = \sqrt{\beta^*}$ is a model constant, ω is the turbulence dissipation rate, k_e is the specific turbulent kinetic energy given by (5), S is the tensor invariant of the strain rate tensor given by (5) and F_2 is a superposition function given by (6):

$$k_e = \frac{u_i u_i}{2} \tag{5}$$

$$S = \sqrt{2 S_{ij} S_{ij}}, \quad S_{ij} = \frac{1}{2}\left(\frac{\partial u_i}{\partial x_j} + \frac{\partial u_j}{\partial x_i}\right) \tag{6}$$

$$F_2 = \tanh\left\{\left[\max\left(\frac{2\sqrt{k_e}}{\beta^* \omega y}, \frac{500\nu}{y^2 \omega}\right)\right]^2\right\} \tag{7}$$

while u_i the fluctuating component of the velocity field and y is the shortest distance to the wall.

The turbulent thermal diffusivity is related to the turbulent kinematic viscosity through the density and turbulent Prantl number (8):

$$\alpha_T = \frac{\rho \nu_T}{Pr_T} \tag{8}$$

The transport equations for the specific turbulent kinetic energy and turbulence dissipation rate are given by (9) and (10):

$$\frac{Dk_e}{Dt} = P_k - \beta^* k_e \omega + \frac{\partial}{\partial x_j}\left[(\nu + \sigma_k \nu_T)\frac{\partial k_e}{\partial x_j}\right] \tag{9}$$

$$\frac{D\omega}{Dt} = \alpha_k S^2 - \beta_k \omega^2 + \frac{\partial}{\partial x_j}\left[(\nu + \sigma_{\omega 1}\nu_T)\frac{\partial \omega}{\partial x_j}\right] + 2(1-F_1)\sigma_{\omega 2}\frac{1}{\omega}\frac{\partial k_e}{\partial x_i}\frac{\partial \omega}{\partial x_i} \tag{10}$$

In (10), P_k is the energy production term given by (11) and F_1 is the superposition function given by (12):

$$P_k = \min\left(\tau_{ij}\frac{\partial U_i}{\partial x_j}, 10\beta^* k_e \omega\right) \tag{11}$$

$$F_1 = \tanh\left\{\left\{\min\left[\max\left(\frac{\sqrt{k_e}}{\beta\omega y}, \frac{500\nu}{y^2\omega}\right), \frac{4\sigma_{\omega 2}k_e}{CD_{k\omega}y^2}\right]\right\}^4\right\} \tag{12}$$

where τ_{ij} is the Reynolds stress tensor and $CD_{k\omega}$ is another superposition function given by (13):

$$CD_{k\omega} = \max\left(2\rho\sigma_{\omega 2}\frac{1}{\omega}\frac{\partial k_e}{\partial x_i}\frac{\partial \omega}{\partial x_i}, 10^{-10}\right) \tag{13}$$

The constants α_k, σ_k and β_k are given as functions of F_1 in (14):

$$\begin{aligned} \alpha_k &= \alpha_{k1}F_1 + \alpha_{k2}(1-F_1) \\ \sigma_k &= \sigma_{k1}F_1 + \sigma_{k2}(1-F_1) \\ \beta_k &= \beta_1 F_1 + \beta_2(1-F_1) \end{aligned} \tag{14}$$

and α_{k1}, α_{k2}, σ_{k1}, σ_{k2}, $\sigma_{\omega 1}$, $\sigma_{\omega 2}$, β_1 and β_2 are constants for the model.

3 Numerical approach

Equations 1–14 were built-in ANSYS CFX 12, a commercially available CFD software package. This CFX software package utilizes a high resolution advection scheme, in which a correction factor applied to the advection term of the variable of interest is calculated at each node so that the resulting scheme is as 2nd order accurate as possible. Transient terms are calculated with a Second Order Backward Euler scheme with automatic time step initialization, in which results from the last and next-to-last time steps are used to calculate the current value of the variable of interest. Pressure coupling is accomplished by a Rhie–Chow algorithm which utilizes the discretized momentum equation at 2 adjacent grid nodes to obtain an expression for the pressure-corrected velocity at the cell face that lie in between the nodes.

Time steps were selected as a fraction of the pulsing period of the membrane. For each simulation, the time step applied corresponded to 1/400 of the period of actuation, which resulted in velocity field RMS residuals smaller than 10^{-8}. Each simulation was set to run through at least 3 pulsing cycles, after which the result jet was considered to be stabilized and average data was extracted over the last pulsing cycle. Time-averaged data planes were examined through the CFX-Post module and data were extracted for use in spreadsheets and EES subroutines.

The 2-D computational domain is seen schematically on Fig. 1. A 2-D geometry was selected in order to allow direct comparison of the commercial CFD software package to previous work [20], which utilized a 2-D model with a highly accurate proprietary spectral method. The 2-D geometry also reduced the computational cost and time of each run, as well as data storage requirements. The streamwise x-direction is defined as the longitudinal jet dimension while the spanwise y-direction is the transversal jet dimension. The computational domain is divided in 3 regions: jet cavity, jet throat and external region. All dimensions are normalized with respect to the throat or orifice diameter D. The cavity region measures $D_m/D = 11.12$ in width and $H_C/D = 2.78$ in height while the throat region has a length

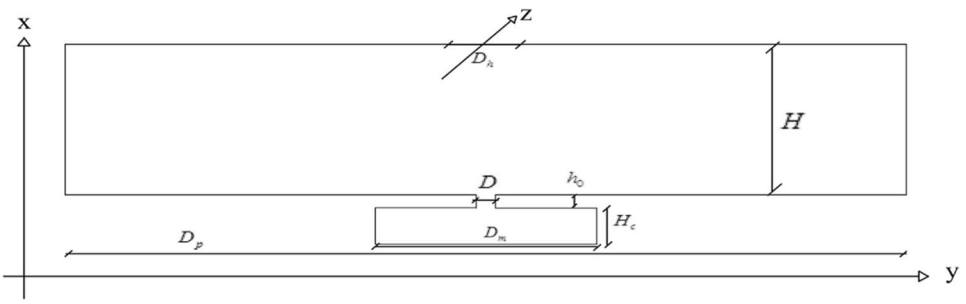

Fig. 1 Schematic of 2-D computational domain

of $h_0 = 0.5D$. The external region has a height H which was one of the varying factors of the parametric study. This region is bounded on the top with a flat surface but open along the left and right boundaries. The width of this external region (D_P) also varies according to the test case but was kept considerably wide, at least 10 times the height of the region (H). This was deliberately selected in order to prevent any pressure or flow condition imposed along the left and right open boundaries to substantially affect the jet at the center of the domain. A heated plate of width D_H is placed directly over the jet orifice. Test cases were conducted in which the distance between the heated plate and the jet orifice (H) was varied through 3, 6, 9, 18 and 24D. Excising the geometric parameter studies, the cavity and heated region widths were maintained proportionally constant at 11.12 and 1.428D, respectively. It should be noted that the actual computational domain was only half of the width seen on Fig. 1 with a symmetry boundary condition applied along the centerline.

The physical and performance parameters considered for the synthetic jet are the jet Reynolds number and Strouhal number. Initially, an average length of column of fluid ejected over the blowing phase is defined according to Eq. (15):

$$L_0 = \int_0^{\tau/2} u_0(t)\mathrm{d}t \tag{15}$$

where τ is the period of actuation of the membrane and u_0 is the time-varying velocity in the exit plane of the jet orifice. The velocity u_0 was obtained by imposing a time-varying velocity along the membrane position and applying the continuitiy equation between the cavity and throat regions. This membrane boundary condition was selected over an actual moving mesh in order to better cope with the amplitudes necessary to produce the range of Re considered in this study. To better emmulate the effect of an actual membrane, the magnitude of the imposed velocity was shaped with a sinusoidal function so that it would be zero at the corners and a maximum at the center of the membrane. Based on L_0, the average jet velocity U_0 during the blowing phase can be defined as:

$$U_0 = \frac{L_0}{\tau} \tag{16}$$

The jet Reynolds number is then defined based on the orifice diameter (D) as shown in Eq. (17):

$$Re = \frac{\rho D U_0}{\mu} \tag{17}$$

while the jet Strouhal number was defined according to pulsing frequency (f) as seen in Eq. (18):

$$St = \frac{2\pi f D}{U_0} \tag{18}$$

Table 1 Geometric and property variations for parametric study

Heated plate distance	3, 6, 9, 18, 24 D
Prandtl number	6, 17
Jet Reynolds number	300, 1200
Plate heating method	Specified heat flux or temperature
Pulsing frequencies	Steady, 1, 4, 100, 200, 400 Hz

Test cases were also performed with two fluids with distinct Prandtl numbers representative of water and ethylene. Jet Reynolds numbers, based on the average orifice jet velocity over the blowing phase were 300 and 1200. Additionally, each combination of geometric and flow parameters was tested with pulsing frequencies of 1, 4, 100, 200 and 400 Hz. Heat flowed into the computational domain through the heated surface by means of a constant heat flux or by imposing a constant higher temperature in this boundary region when compared to the temperature imposed at the domain open boundaries and initial fluid temperature. Table 1 contains a list of all parameters utilized in this study. Not all permutations of parameters were tested but, in all, 66 simulations were conducted in order to collect sufficient data to determine the heat transfer correlation.

3.1 Validation and grid convergence study

Validation of the current numerical method was performed by comparing results with theoretical steady jet profiles and other numerical work involving synthetic jets. Detailed validation and grid convergence results are presented in [21] and are summarized in this section. The geometry used for this part of the study differed from the one shown on Fig. 1. Since the experimental work of [1] was performed on a free jet, the equivalent computational domain would have to be considerbaly longer in the longitudinal x-direction. However, conforming to this requirement and maintaining the same external domain width would result in a computational mesh excessively large. Therefore, the external domain used here was modified to have a height H/D of 21.8 but relatively narrow width D_P/D of 16.67. The computational mesh contained initially approximately 240,000 elements with grid refinement around corners and regions of high shear.

For a steady, turbulent, 2-D jet, the time-averaged jet centerline velocity (U_{cl}) was found to be in good agreement with the experimental data of [1] in regions beyond $x/D > 10$ with a decay of $x^{-0.58}$. The resulting jet width, measured as the location where the average longitudinal jet velocity is $0.01U_{\mathrm{cl}}$, was similarly in agreement with the experiments of [1] with a growth proportional to $x^{0.88}$ for regions away from the orifice exit plane. Similar to a steady jet, normalizing the average longitudinal velocity profiles (U) at different

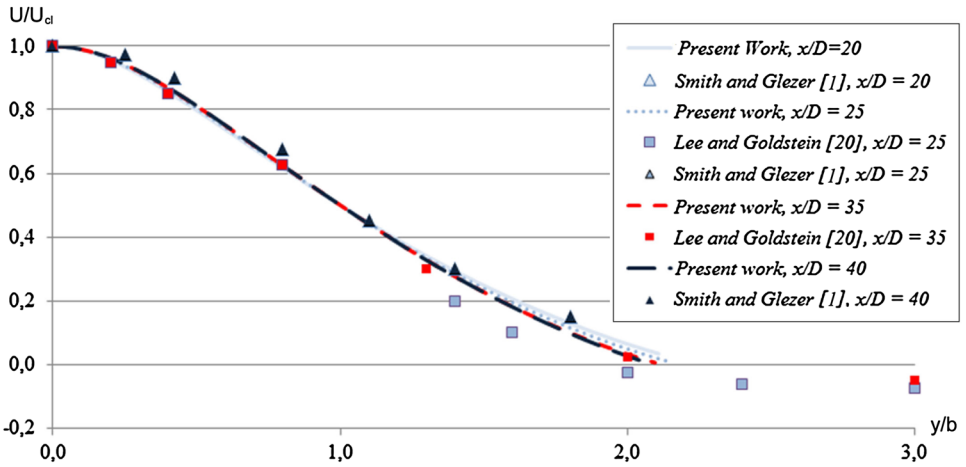

Fig. 2 Comparison of normalized longitudinal jet velocity at different stations between current work and references

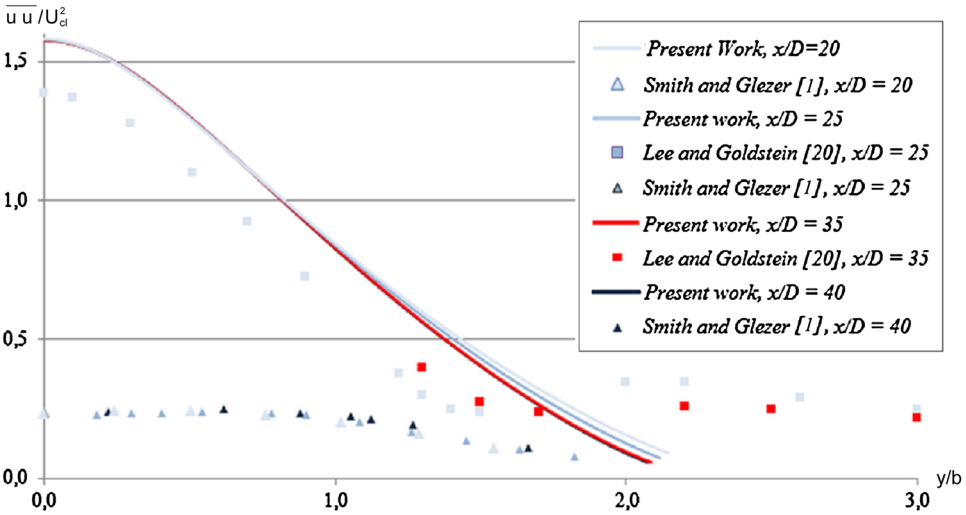

Fig. 3 Comparison of normalized longitudinal velocity self-correlation at different stations between current work and references

x-stations with respect to the U_{cl} and jet width resulted in self-similar profiles as seen in Fig. 2. The self-similar profiles also show good agreement of the current results with the experimental data of [1] and numerical work of [20]. However, as seen in Fig. 3, profiles of the self correlation of the fluctuation of longitudinal velocity ($\overline{uu}$) overpredicts the experimental fluctuation of [1]. This result was not surprising since it was also observed in [20] and is attributed to the nature of a 2-D simulation, which does not include the additional spanwise turbulent breakdown of an actual jet.

Grid convergence was checked by comparing the baseline grid with two other cases: a grid containing 150 % more elements and another doubling the grid size. Results on the jet velocities and width growth were compared in between the meshes and grid-independent results were determined to occur with the 150 % grid. The smallest grid spacing, which corresponded to a longitudinal gridcell Re of 16.58 at the throat region of the orifice was then transfered over to the grid of Fig. 1 and utilized in the remainder of this study.

4 Velocity and temperature fields

Since the domain of Fig. 1 consists of a jet impacting a near surface, it is of interest to describe the general characteristics of the velocity and temperature fields that result with this geometry. As expected for jets in a confined space, the ejected fluid impacted against the upper domain, flowing outwards and backwards to form a circulation cell. This result is illustrated on Fig. 4, through the time-averaged contours of normalized vorticity (Ω_{avg}) for the case $H/D = 9$, $Re = 1200$ and $Pr = 6$. The left side of Fig. 4 corresponds to a steady jet while the right side corresponds a synthetic jet of frequency 100 Hz. As seen on the left side, the steady jet forms a well defined circulation cell spanning the height of domain H and measuring approximately $1.5H$ in width. The synthetic jet on the right side also forms an average circulation cell but with a more fragmented vortical structure. Additionally, although the synthetic cell spans the height of the domain, it is wider than the steady jet cell, measuring approximately $2H$.

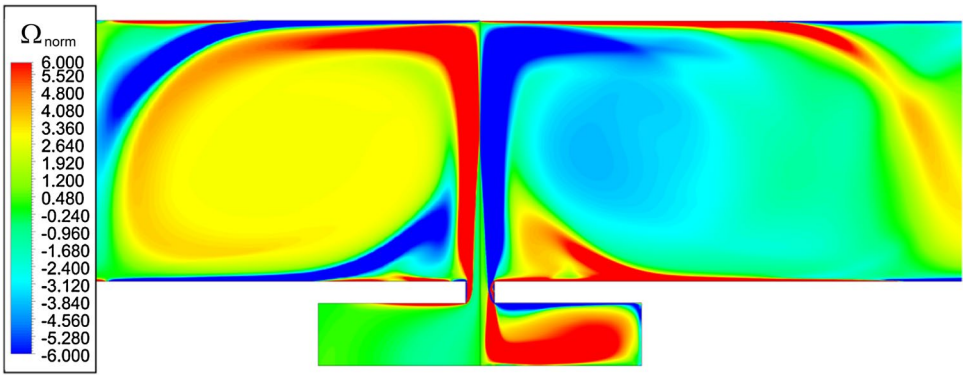

Fig. 4 Time averaged vorticity contours for $H/D = 9$, $Re = 1200$ and $Pr = 6$ for pulsating jet of frequency = 100 Hz (*right*) and steady jet (*left*) after 1 period of actuation

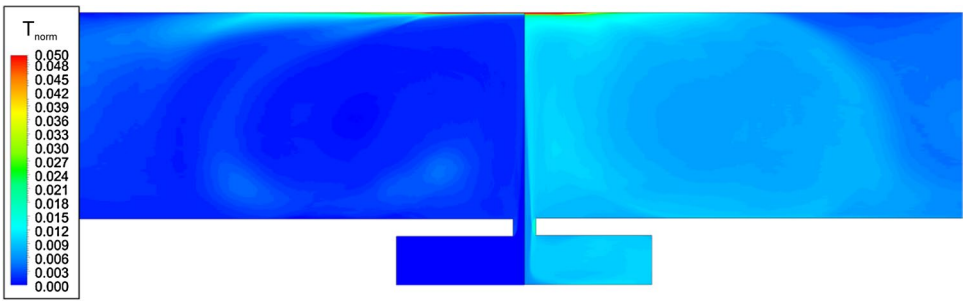

Fig. 5 Instantaneous normalized temperature contours for $H/D = 9$, $Re = 1200$ and $Pr = 6$ for pulsating jet of frequency = 100 Hz (*right*) and steady jet (*left*) after 1 period of actuation

The steady jet circulation cell on the left side of Fig. 4 is representative of other steady jet studies [22]. The circulation cell itself is well defined, which is a result of the combination of shallow height of the domain and jet Reynolds number. The steady jet time-averaged vorticity remains intense within the core of the jet and within the impingement zone. As the vorticity layer is deflected along the top wall and rolls up in a circulation cell, it gradually fades in intensity—an expected effect since the turbulence mechanism is no longer fed by shearing of the no-slip top wall. In comparison, the synthetic jet circulation cell on the right of Fig. 4 contains higher levels of turbulence both within it and in the impingement zone which results in larger heat dissipation. However, as seen on the figure, the oscillating nature of the jet destabilizes the flow along the top wall enough to detach the impacting (blue) vorticity layer. As a result, a secondary, but equally intense (red) vorticity layer is created with the opposite rotation of the impacting (blue) vorticity layer. This secondary (red) vorticity layer drags fluid toward and further along the wall until viscous effects causes it to roll up in a circulation cell. The combination of fragmented vorticity layer and fluid being dragged along the top wall are thus the reason for the fragmented and wider shape of the synthetic jet circulation cell when compared to a steady jet.

Thermal results are illustrated on Fig. 5 through instantaneous normalized temperature contours (T_{norm}) for the case $H/D = 9$, $Re = 1200$ and $Pr = 6$, with the steady jet on the left side and the synthetic jet on the right side. Both temperature fields were taken after a period of time equivalent to the end of the first pulsating cycle. Figure 5 illustrates well the mixing nature of a synthetic jet and its positive effect on heat dissipation. After this short time interval of operation, the steady jet on the left side of the figure has resulted in minimal mixing of the thermal layer, with the shape of temperature contours corresponding roughly to the forming circulation cell. In contrast, the synthetic jet on the right side of the figure displays considerable mixing as the higher temperature layer near the heated top surface is quickly dissipated and spread over the entire region of the forming circulation cell.

4.1 Geometric parametric study

A parametric study was conducted on geometric parameters such as cavity size and throat shape and length and its effects on the velocity field are reported in this section. Similar studies [8, 20, 23] have been conducted in more detail. However, since it is not feasible to replicate all their results in this study, selected parametric studies were conducted on the more relevant factors.

4.1.1 Cavity depth

The effect of cavity depth was tested by maintaining the straight baseline throat geometry and length $h_0/D = 0.5$ but varying the cavity height. From the baseline cavity height of $2.78D$, a shallower cavity of $0.41D$ and a deep

cavity of 5.57D were tested. These resulted in cavities with width to height ratios of D_m/H_C of 2, 4 and 27.26, respectively. For the time-averaged jet centerline velocity, there was no substantial change for cavities 5.57 and 2.78D deep. However, once the cavity becomes very shallow (0.41D), there is a peak increase of 30 % in average jet centerline velocity for regions very close to the jet orifice ($X/D < 6$) when compared to the original geometry. This increase in U_{cl} gradually tapers off so that at $x/D = 12$ it is halved to 15 %. These results are in agreement with [20] and [23]. For the shallowest cavity tested, Jain et al. [23] observed that the time-varying, area-averaged velocity at the orifice exit plane had higher peak ejection velocities and this value was sustained for a longer period of time compared to deeper cavities while suction velocity profiles were mostly unchanged. Therefore, it is reasonable to assume that the overall time-averaged jet centerline velocity would be higher, which is the result of the present work. Similar results were observed by Lee and Goldstein [20]—an increase in celerity of the ejected vortices of a shallow cavity. Similar effects were observed on the jet width. Cavities 5.57 and 2.78D deep presented little difference on the jet width growth. However, for the very shallow cavity of 0.41D, there is a distinct change in behavior. For near regions ($x/D < 5$), the 0.41D cavity jet starts out 28 % narrower than the other cases but progressively approaches similar jet widths as x/D increases. This trend reverses for distances $x/D > 5$ and the 0.41D cavity jet becomes increasingly wider with respect to the baseline geometry. At the last data point examined ($x/D = 12$), the 0.41D cavity jet has become 33 % larger than the other geometries tested. The narrow near region jet width can be related to the increase in U_{cl}. The higher velocity and momentum in the near region allows the jet to maintain its coherent shape and retard the natural expansion of the shear layer. The trend reversion can be explained by the presence of the upper boundary placed on the domain as shown in the contours of Fig. 6. Figure 6 shows average vorticity contours for both the baseline case (left) and shallow cavity (right). The higher average velocity of the narrow cavity jet impacts the upper boundary with higher momentum and forms a larger circulation cell than the baseline case. The lower pressure associated with a vortical structure would naturally draw fluid towards it, thus affecting the jet width.

4.1.2 Throat shape and length

The effect of throat shape was examined by changing the baseline straight geometry with a converging straight throat at a 45° angle. The overall orifice throat length and the cavity depth were maintained as the baseline case ($h_0/D = 0.5$, $D_m/D = 11.12$ and $H_c/D = 2.78$). For the time-averaged jet centerline velocity, the 45° angled throat resulted in an average jet centerline velocity around 80 % higher than the baseline geometry. This result remained fairly constant up to a distance of $X/D = 12$ and is a direct result of the accelerating converging duct effect in an incompresible fluid. However, the effects of throat shape on the jet width were found to be minor. Overall, the jet width between the 45° angled throat and the original geometry

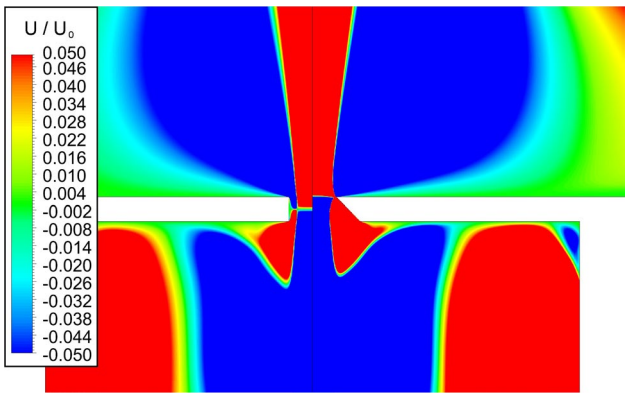

Fig. 7 Time-averaged normalized velocity contours for baseline throat (*left*) and 45 angled throat (*right*)

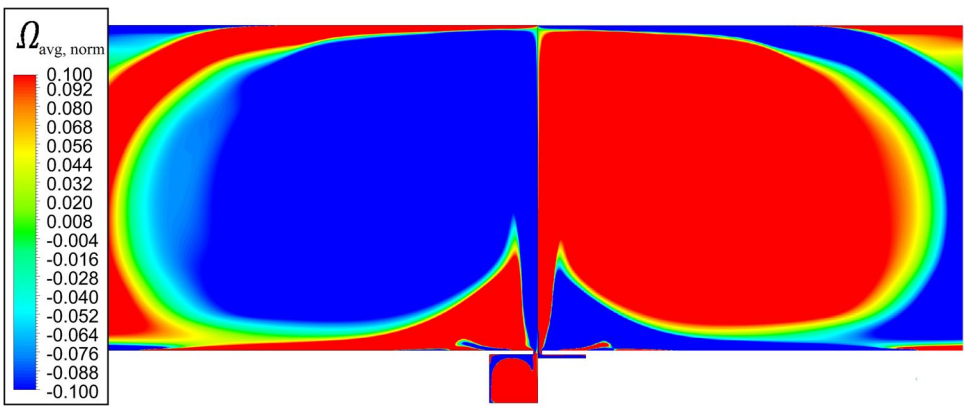

Fig. 6 Time-averaged normalized vorticity contours for baseline cavity (*left*) and shallow cavity (*right*)

were found to be nearly unchanged through most of the x/D positions tested. Only at a distance of $x/D = 12$, the 45° angled throat presented a slight decrease of 3 % with respect to the original geometry. The effects of throat geometry on the velocity field can be seen through the time-averaged velocity contours of Fig. 7. As seen on Fig. 7, the angled shape not only naturally accelerates the flow but also avoids an abrupt separation of the cavity flow on the inner sharp lip edge seen in the straight baseline geometry. The contours also show that the near-region jet for the 45° angled throat has a more curved shape compared to the baseline case. This effect can be explained by the fact that the angled shape of the throat redirects the flow towards the centerline. The left contours of Fig. 7 also show that the average flowfield forms a stagnation plane at the center of the straight throat. In contrast, the right contours show that, for the 45° angled throat, the stagnation plane forms at the exit plane.

The effect of throat length was examined by maintaining the straight throat geometry and baseline cavity size ($D_m/D = 11.12$ and $H_c/D = 2.78$). However, the baseline throat length of $h_0/D = 0.5$ was compared to a short geometry of only $h_0/D = 0.05$. Results on the time-averaged jet centerline showed an initial increase in U_{cl} of around 20 % which, decreased slightly so that, at $x/D = 12$, it was only 10 % highter than the baseline value. These results differ from [20], which observed a gradual increase in U_{cl} with increasing throat length due to hydraulic contraction brought on by the development of an entry-region type flow. However, it should be noted that [20] compared several throat lengths starting from an infinitely thin throat up to a width of $h_0/D = 2.5$. In comparison, the two geometries tested here would both be considered short lengths. Effects on the jet width were minimal and similar to the throat geometry study: throughout most of distances examined, jet width growth was similar between the two geometies. Only at the furthermost location of $x/D = 12$ the sharp cavity presented a slight increase of 2.6 % with respect to the original geometry.

4.2 Heat transfer effects and Nusselt number correlation

Heat transfer studies were conducted on the baseline geometry of a straight throat of height $h_0 = 0.5D$ and a cavity of width $D_m/D = 11.12$ and height $H_C/D = 2.78$. The height of the extenal domain (H) was varied from values of $3D$ up to $24D$. Regardless of the heating method (constant temperature or constant heat flux), the Nusselt number was calculated by extracting rows of data from the average temperature field at and near the heated region and equating the heat flux leaving the wall with the convective heat flux gained by the fluid. Due to the large amount of data accumulated, only selected results are displayed in this section to illustrate the results obtained in this study. Figures generated for these synthetic jet results were time averaged over the third pulsating cycle and compared to steady jet cases of equivalent jet Reynolds numbers allowed to reach a steady state. Thus, while the steady jet cases can be considered to have been converged in time, the same cannot be necessarily assumed for the synthetic jets. However, the results obtained in this study are consistent with other numerical studies. Sample results are shown in Figs. 8 and 9. Figure 8 shows results for a jet of $Re = 300$ in a fluid with $Pr = 6$ with varying distances H/D between the heated plate and jet orifice and different pulsing frequencies. Figure 9 shows the results for the same conditions but with a jet of $Re = 1200$.

Figures 8 and 9 show results consistent with the experiments of [9], in that Nu gradually decreases from a maximum value as H/D increases. Additionally, [9] showed that, depending on the configuration of the test case, a maximum value of Nu is reached in a region of H/D between 3 and 9. This result was not observed in the present results due to the lack of a test case below $H/D < 3$. Figures 8 and 9 also shows that Nu increases with pulsing frequency, as observed in the experiments of [9]. Figure 8 shows that, for a Re of 300, a pulsing frequency of 100 Hz results in a Nu as much as 43 % larger than for a steady jet when the heated

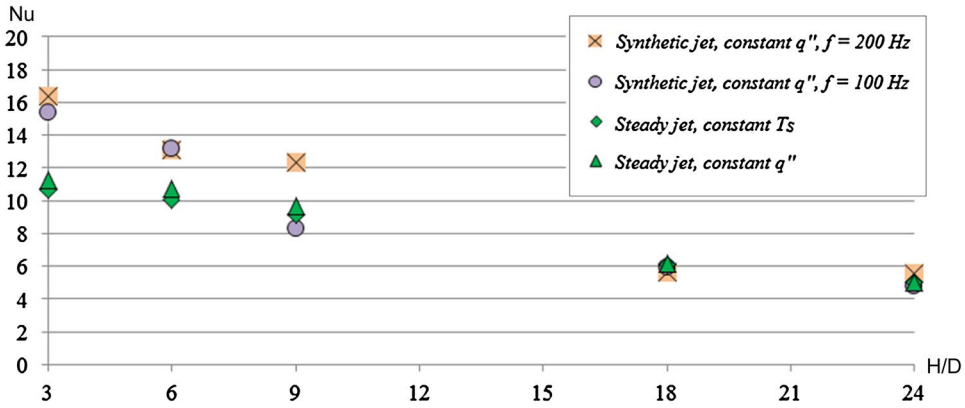

Fig. 8 Nusselt number for jets with $Re = 300$ and fluid with $Pr = 6$ with varying distances between the heated plate and jet orifice

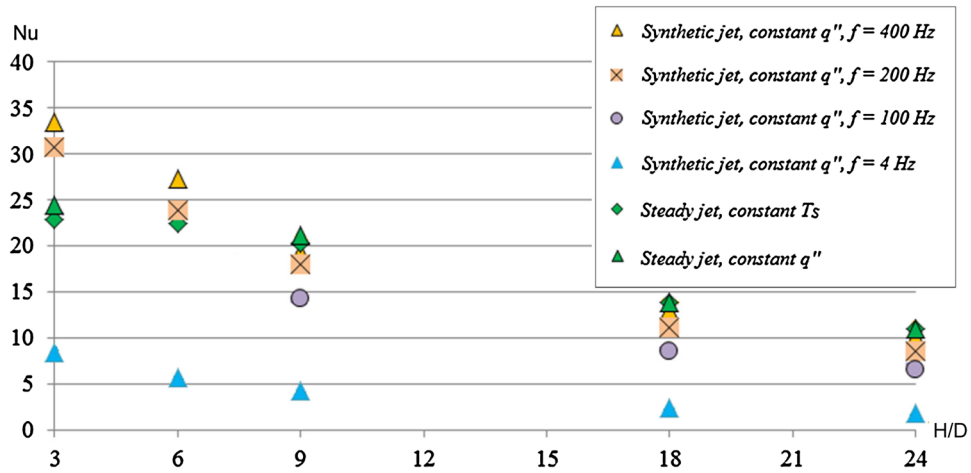

Fig. 9 Nusselt number for jets with $Re = 1200$ and with fluid $Pr = 6$ with varying distances between the heated plate and jet orifice

surface is in the near region of the jet orifice ($x/D < 12$). However, this improvement in *Nu* sharply drops and for a heated surface at $H/D = 18$ there is no significant difference between the synthetic and steady jet. In contrast, Fig. 9 shows that at a *Re* of 1200, a pulsing frequency of 100 Hz is insufficient for the synthetic jet to outperform a steady jet. However, increasing the pulsing frequency to 200 Hz resulted in a *Nu* 40 % larger for the syntehtic jet but its drop was even sharper than as seen at the lower *Re*. At a distance of $H/D = 9$ the *Nu* gains by the syntehtic jet are no longer present and the location of this sharp drop remains the same even as the pulsing frequency is raised to 400 Hz. It should be noted that due to the nature of the incompressible simulation, which lacks a real physical membrane and a finite speed of sound in the fluid, the two critical resonating frequencies noted in [17] do not exist here. Consequently it is expected that *Nu* values would continuously rise with pulsing frequency.

Table 2 Coefficients for Nusselt number correlation

	0	1	2	3
A	1.030	–3.967	–2,561	–
B	1.791	1.320	1.136	–
C	–2.783	–1.967	–1.873	0.131
b	0.162	–1	–0.6419	–
c	–1	–0.0635	0.4966	–0.9709

The aggregated data from all test cases was collected to form an error minimization problem. It was assumed that a correlation of *Nu* exists involving *Re*, *Pr*, *St* and H/D with the format of Eq. (19):

$$Nu_{(\mathrm{corr})} = A_0 + \left[\left(St^{b_0} + B_0\right)\left(Re^{b_1} + B_1\right)\left(Pr^{b_2} + B_2\right) + A_1\right] \times \left\{\left[\left(\frac{H}{D}\right)^{c_0} + C_0\right]\left(St^{c_1} e + C_1\right)\left(Re^{c_2} + C_2\right)\left(Pr^{c_4} + C_3\right) + A_2\right\} \tag{19}$$

where all constants A through C and a through g are to be determined. For each test case i, the residual was calculated by Eq. (20) as the difference between the correlation and test case:

$$\mathrm{Residual}_{(i)} = Nu_{(\mathrm{corr})} - Nu_{(i)} \tag{20}$$

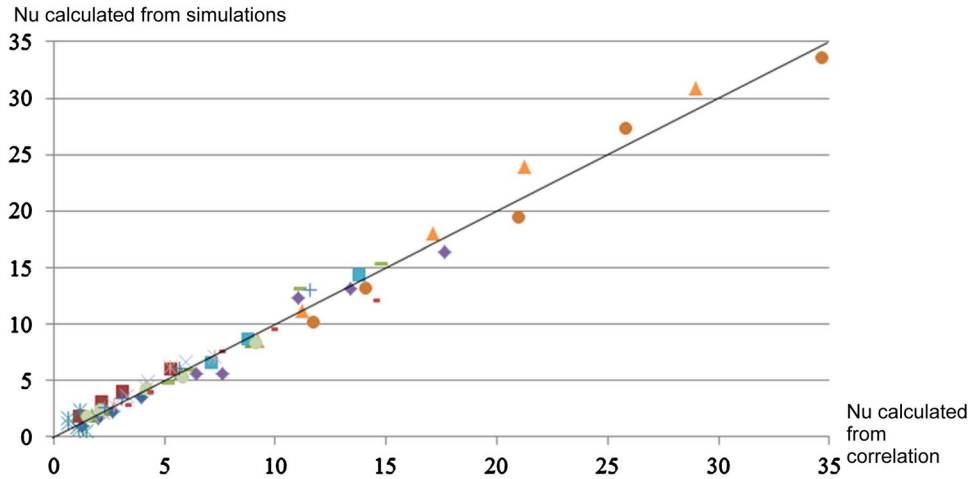

Fig. 10 Nusselt number for jets with $Re = 1200$ and $Pr = 17$ with varying distances between the heated plate and jet orifice

and the total residual is the RMS of all residuals is given by (21):

$$\text{Residual} = \sqrt{\sum_{\text{all}} \left(\text{Residual}_{(i)}^2\right)} \tag{21}$$

All data was inserted in EES (Engineering Equation Solver), a comercially available equation solver software, in order to determine the values of all coefficients that would result in the minimum RMS of the global residual. Based on all 66 test cases of this study, the minimization problem yielded the coefficients shown on Table 2. The relative quality of the correlation can be glimpsed in Fig. 10, which shows a sampling of 15 test cases comparing the calculated values of *Nu* from field data and the correlation of Eq. (). For comparison purposes, a trendline of slope 1:1 is shown along the diagonal. The plotted data on Fig. 10 show that the correlation has resulted in a reasonable spread of data about the trendline.

5 Conclusions

The problem of impingement cooling with a single synthetic jet was studied numerically with commercially-available scientific software. Validation with experimental results and other numerical studies show the suitability of the chosen numerical method and turbulence model to represent the characteristics of free 2-D steady and synthetic jets. A parametric study on geometric parameters indicated that cavity depth bore a significant effects on the jet time-averaged centerline velocity and width. Changes to the shape and length of the throat region produced effects only on the time-averaged centerline velocity while the jet width remained nearly unchanged. For the heat transfer results, a geometry of a semi-confined jet, with a heated plate placed directly above and at relatively close distances to the orifice was utilized. Time-averaged results show that a synthetic jet is able to form a periodic circulation cell within 3 periods of actuation in the region of interest. Instantaneous results show that, unlike the steady jet, the synthetic jet is able to induce substantial mixing from the first emitted pulse. However, later results confirmed that the thermal dissipation performance of the synthetic jet depends on several factors, with the distance between the orifice and the plate and the pulsing frequency being the most influential. Calculated Nusselt numbers showed peak values when the heated surface was placed close to the orifice with sharp drops as this distance was increased. Very low pulsing frequencies resulted in *Nu* far below values for equivalent steady jets. Only at higher pulsing frequencies (100–200 Hz) were synthetic jets found to be comparable or superior to a steady jet. Moreover, the pulsing frequency necessary for the synthetic jet to outperform steady jets increases with jet Reynolds numbers. The size of this optimum region for the synthetic jet also tended to shrink as the jet Reynolds number increased. At the highest jet Reynolds numbers tested, this region was limited to below 9*D*. A total of 66 test cases were performed, with variations both in geometry, pulsing frequency, *Re* and *Pr*. The results were utilized to determine the coefficients of a correlation for *Nu* based on these parameters that do not require full knowledge of the temperature field. Comparison to the test cases show good agreement for this correlation, making it a valuable tool in the analysis of this type of heat transfer problem.

Acknowledgments This work is supported by the Unisinos Office of Research and Graduate Studies and Fundação Padre Milton Valente.

References

1. Smith BL, Glezer A (1998) The formation and evolution of synthetic jets. Phys Fluids 10(9):2281–2297
2. Mallinson SG, Reizes JA, Hong G (2001) An experimental and numerical study of synthetic jet flow. Aeronaut J 105:41–49
3. Crook A, Sadri AM, Wood NJ (1999) The development and implementation of synthetic jets for control of separated flow. In: Proceedings of AIAA paper 99–3176, AIAA 17th applied aerodynamics conference, Reno, NV, pp 99–3176
4. Chen FJ, Yao C, Beeler GB, Bryant RG, Fox L (2000) Development of synthetic jet actuators for active flow control at NASA Langley. In: Proceedings of AIAA paper 2000–2405, AIAA fluids meeting conference, Denver CO
5. Zhang P, Wang JJ, Feng L (2008) Review of zero-net-mass-flux jet and its application in separation flow control. Beijing University of Aeronautics and Astronautics, Institute of Fluid Mechanics, Beijing, China
6. Saffman PG (1981) Dynamics of vorticity. J Fluid Mech 106:49–58
7. Auerbach D (1987) Experiments on the trajectory and circulation of the starting vortex. J Fluid Mech 183:185–198
8. Chaudhari M, Puranik B, Agrawal A (2010) Effect of orifice shape in synthetic jet based impingement cooling. Exp Thermal Fluid Sci 34:246–256
9. Chaudhari M, Puranik B, Agrawal A (2010) Heat transfer characteristics of synthetic jet impingement cooling. Int J Heat Mass Transf 53:1057–1069
10. Etemoglu AK (2007) A brief survey and economical analysis of air cooling for electronic equipments. Int Comm Heat Mass Transf 34:103–113
11. Pavlova A, Amitay M (2006) Electronic cooling using synthetic jet impingement. J Heat Transf 128(9):897–907
12. Gillespie MB, Black WZ, Rinehart C, Glezer A (2006) Local convective heat transfer from a constant heat flux flat plate cooled by synthetic air jets. J Heat Transf 128:990–1000
13. Mahalingam R, Glezer A (2002) Air cooled heat sinks integrated with synthetic jets. IEEE inter society conference on thermal phenomena, pp 285–291
14. Mahalingam R, Glezer A (2005) Design and thermal characteristics of a synthetic jet ejector heat sink. J Elec Pack 127(1):172–177

15. Mahalingam R, Rumigny N, Glezer A (2004) Thermal management using synthetic jet ejectors. IEEE 27(3):439–444
16. Erbas N, Baysal O (2009) Micron-level actuators for thermal management of microelectronic devices. Heat Transf Eng 30(1–2):138–147
17. Chaudhari M, Verma G, Puranik B, Agrawal A (2009) Frequency response of a synthetic jet orifice. Exp Thermal Fluid Sci 33:439–448
18. Garg J, Arik M, Weaver S (2005) Meso-scale pulsating jets for electronics cooling. J Elec Pack 127(4):503–512
19. Menter FR (1994) Two-equation eddy-viscosity turbulence models for engineering applications. AIAA J 32(8):1598–1605
20. Lee CYY, Goldstein DB (2002) Two-dimensional synthetic jet simulation. AIAA J 40(3):510–516
21. Lehnen MV, Lee CYY (2012) Characterization of physical parameters on the performance of synthetic jets. In: Proceedings of CONEM paper 2012–0938, VII Congresso Nacional de Engenharia Mecnica, São Luis, MA, Brazil
22. Caggese O, Gnaegi G, Hannema G, Terzis A, Ott P (2013) Experimental and numerical investigation of a fully confined impingement round jet. Int J Heat Mass Transf 65:873–882
23. Jain M, Puranik B, Agrawal A (2011) A numerical investigation of effects of cavity and orifice parameters on the characteristics of a synthetic jet flow. Sens Actuators A 165:351–366